Photoelectron spectra of alkali metal–ammonia microjets: From blue electrolyte to bronze metal

Tillmann Buttersack[1,2]*, Philip E. Mason[1]*, Ryan S. McMullen[2]*, H. Christian Schewe[3]*, Tomas Martinek[1], Krystof Brezina[1,4], Martin Crhan[1], Axel Gomez[1,5], Dennis Hein[6,7], Garlef Wartner[6,7], Robert Seidel[6,7], Hebatallah Ali[3], Stephan Thürmer[8], Ondrej Marsalek[4]†, Bernd Winter[3]†, Stephen E. Bradforth[2]†, Pavel Jungwirth[1]†

[1]Institute of Organic Chemistry and Biochemistry, Czech Academy of Sciences, Flemingovo nám. 2, 16610 Prague 6, Czech Republic. [2]Department of Chemistry, University of Southern California, Los Angeles, CA 90089-0482, USA. [3]Molecular Physics, Fritz-Haber-Institut der Max-Planck-Gesellschaft, Faradayweg 4-6, D-14195 Berlin, Germany. [4]Charles University, Faculty of Mathematics and Physics, Ke Karlovu 3, 121 16 Prague 2, Czech Republic. [5]Département de Chimie, École Normale Supérieure, PSL University, 75005 Paris, France. [6]Helmholtz-Zentrum Berlin für Materialien und Energie, Albert-Einstein-Strasse 15, D-12489 Berlin, Germany. [7]Department of Chemistry, Humboldt-Universität zu Berlin, Brook-Taylor-Str. 2, D-12489 Berlin, Germany. [8]Department of Chemistry, Graduate School of Science, Kyoto University, Kitashirakawa-Oiwakecho, Sakyo-Ku, Kyoto 606-8502, Japan.
*These authors contributed equally to this work.
†Corresponding author. Email: ondrej.marsalek@mff.cuni.cz (O.M.); winter@fhi-berlin.mpg.de (B.W.); stephen.bradforth@usc.edu (S.E.B.); pavel.jungwirth@uochb.cas.cz (P.J.)

Experimental studies of the electronic structure of excess electrons in liquids—archetypal quantum solutes—have been largely restricted to very dilute electron concentrations. We overcame this limitation by applying soft x-ray photoelectron spectroscopy to characterize excess electrons originating from steadily increasing amounts of alkali metals dissolved in refrigerated liquid ammonia microjets. As concentration rises, a narrow peak at ~2 electron volts, corresponding to vertical photodetachment of localized solvated electrons and dielectrons, transforms continuously into a band with a sharp Fermi edge accompanied by a plasmon peak, characteristic of delocalized metallic electrons. Through our experimental approach combined with ab initio calculations of localized electrons and dielectrons, we obtain a clear picture of the energetics and density of states of the ammoniated electrons over the gradual transition from dilute blue electrolytes to concentrated bronze metallic solutions.

Since the discovery of spectacularly colored alkali metal–ammonia solutions in the early 19th century, excess ammoniated electrons have attracted considerable attention, as reviewed recently by Zurek et al. (1) [seeThompson's classicmonograph (2) for an overview of the older literature]. Alkali metals are soluble in liquid ammonia up to concentrations of roughly 20 mol % metal (MPM)—i.e., one metal atom per about four solvent molecules (1). A transition from a blue electrolyte to a bronze- or gold-colored metallic solutionupon increasing alkali metal concentration is accompanied by a liquid–liquid phase separation at sufficiently low temperatures (1–7). The nature of themetallic transition in both liquid and crystalline alkali metal–ammonia systems, directly evidenced by an orders-of-magnitude increase in electrical conductivity, has puzzled researchers for decades (1, 8–10) and is not yet understood in molecular detail. The involved chemical species include dilute solvated electrons and dielectrons as well as their various complexes with alkali metal cations (1)—all gradually coalescing into delocalized structures and giving rise to a conduction band. A series of conferences on this topic, the Colloques Weyl, was organized in the second half of the past century, resulting in a series of articles primarily focused on the structure, thermodynamics, and electrical and magnetic properties of the alkali metal–ammonia solutions (11–16). Electrons in liquid ammonia have also been thoroughly studied with nuclear magnetic resonance (NMR) and electron spin resonance (ESR) techniques. The latter show a narrow structureless spin resonance line with a g value (i.e., dimensionlessmagneticmoment) characteristic of a free-electron spin, which broadens upon increasing the alkali metal concentration (2, 17). Shifts in the 1H and 14NNMR positions (Knight shifts) give a measure of the unpaired electron spin density at all constituent nuclei within the orbit of the molecules solvating the unpaired electron (17, 18). Shkrob has argued (19) that the Knight parameters from14NNMR, electron spin echo relaxation, and ESR linewidth data can only be interpreted as a transfer of a substantial fraction of the spin density to the nitrogen atoms in the first solvent sphere.

The principal means to explore electronic structure, and thus the binding energies and density of states of excess ammoniated electrons, is photoelectron spectroscopy (PES). Liquid ammonia has a great advantage over water in that high concentrations of ammoniated electrons can be reached in solutions that are stable for extended periods of time without the danger of explosion (20). Nevertheless, compared with the number of such investigations of electrons solvated in water (i.e., hydrated electrons) (21–23), PES studies in liquid ammonia are scarce. Early photoelectron (PE) total emission yield experiments led to an estimate of the PE threshold of ~1.4 eV (24, 25), in good agreement with electrochemical determination of the adiabatic binding energy of an ammoniated electron (26). This value is also roughly consistent with results from cluster extrapolations (27–31). However, clusters have only limited relevance to liquid bulk systems, as they inevitably exhibit pronounced surface effects and are typically solid rather than liquid (32, 33). As a result, structures such as metastable clusters exist; these structures are characterized by low electron binding energies and have no liquid bulk analog (33). Electron scattering data from clusters also differ from condensed phase data (34). Additional insight into the ultrafast dynamics of ammoniated electrons emerged from femtosecond time-resolved experiments involving multiphoton photoionization in pure liquid ammonia or photoexcitation in dilute alkalimetal–ammonia solutions (35–38). These studies have typically probed ammoniated electrons in the low-concentration regime (i.e., individual electrons well below the electrolyteto- metal transition). In concentrated systems, plasmons in metallic lithium–ammonia solutions were explored by x-ray scattering two decades ago (10), and a PES study of small to medium-sized cryogenic sodium–ammonia clusters was performed recently (31).

There is thus a clear need for a direct PES investigation of excess ammoniated electrons that would cover both the electrolyte and metallic regimes. We have recently overcome a critical obstacle in collecting PEs from a volatile polar refrigerated liquid. We developed an experimental setup that produces a liquid ammonia microjet and performed PES measurements with this apparatus

(39). In that study, we characterized the valence and core orbital structure of pure gaseous and liquid ammonia and quantified the effect of the condensed phase environment on the orbital energies, which was found to be even stronger than in water, despite weaker hydrogen bonding in liquid ammonia (40). This work has paved the way for PES investigations mapping the electrolyte-to-metal transition through the study of liquid alkali metal–ammonia solutions of increasing concentrations, as reported here.

Electronic structure calculations enable interpretation of PES measurements of ammoniated electrons in terms of a complex structural, dynamical, and molecular orbital picture. So far, only molecular pseudopotential calculations have been performed for electrons in liquid ammonia (41, 42), with density functional theory (DFT) applied to crystalline alkali metal–ammonia systems (8). Although the early liquid-state calculations provided some insight into the transition from individual solvated electrons through dielectrons [which exist as spin-paired singlet species in liquid ammonia (43)] to the onset of delocalized states upon increasing alkali metal loading, these findings were inevitably of a qualitative nature only. This was due to neglect of the explicit electronic structure of the solvent and to approximations made in the pseudopotential itself (33). We have shown previously that, in aqueous solutions, a quantitative picture of the electronic structure of hydrated electrons and surrounding water molecules can be obtained through DFT-based ab initio molecular dynamics (AIMD) (44). In this study, we employed an extension of this approach, combining it with quantum chemical embedded-cluster evaluation of electron binding energies to characterize ammoniated electrons and dielectrons.

Photoelectron spectroscopy: Electrolyte solutions

PE experiments were carried out with the SOL³PES experimental setup (45) at the U49/ 2-PGM-1 beamline at the synchrotron radiation facility BESSY II (46) (for details, see the "Experimental Methodology" section in the supplementary materials). PE spectra at low electron binding energies of microjets of lithium–liquid ammonia solutions at alkali metal concentrations ranging from 0.012 to 9.7 MPM are presented in Fig. 1A. Analogous low-energy spectra of potassium–liquid ammonia solutions (0.15 to 1.25 MPM) and sodium–liquid ammonia (0.15 to 0.75 MPM) are shown in Fig. 1, B and C. Visually, the increase of alkali metal concentration is connected with deepening of the characteristic blue color of the solutions, with the higher concentrations becoming nearly black, even in the thin microjet, and the solution with the highest lithium concentration acquiring a discernible bronze-colored metallic sheen.

Similarly to previously studied aqueous microjets (47, 48), in experiments with liquid ammonia we observed electrostatic effects leading to global PE spectral shifts. These shifts are larger for alkali metals in liquid ammonia than for solutions of alkali halide salts at equivalent concentrations (49). To correct for these instrumental spectral shifts, the low concentration spectra (0.08 MPM for Li and 0.15 MPM for Na and K) were aligned horizontally such that the lowest-energy liquid ammonia peak ($3a_1$), fitted to a Gaussian function, was always anchored at 9.09 eV, which is the value of the corresponding vertical detachment energy (VDE), as determined in our recent PE measurements of a pure liquid ammonia microjet (39). All other spectra were aligned using the same shift. This procedure (see the supplementary materials for more details) is well justified; for low-to-moderate alkali metal concentrations, the effect of ionic solutes on the position of the solvent PE peaks has been found to be negligible in water [see below and (47, 48)]. Nevertheless, these factors combine to produce a small systematic uncertainty in determining absolute values of VDEs, which we estimate not to exceed ~0.4 eV.

A notable result of the present measurements is that from ~0.08 to ~1 MPM the PE spectra consistently show a small but clearly visible peak at a VDE of ~2 eV (Fig. 1). The integrated area of this peak is roughly linearly proportional to the number concentration of the alkali metal (Fig. 1D). The observation that the position of this peak essentially does not depend on the chemical nature of the alkali metal points directly to ammoniated electrons. More precisely, starting from ~10^{-3} MPM, the solvated electrons engage in spin-pairing to form dielectrons (1, 2, 50). ESR measurements provide an estimate of the concentration dependence of the dielectron/electron ratio (2), which increases with dissolved metal concentration and reaches a factor of ~10 around 0.1 MPM. The measured value of ~2 eV thus corresponds primarily to the VDE of dielectrons.

Electronic structure calculations

Our experimental conclusions are further supported by electronic structure calculations. To model the structure of electrons, dielectrons, and electron–alkali cation pairs (fig. S10) in liquid ammonia, we need to go beyond both static ab initio calculations of small clusters (51) and molecular pseudopotential bulk simulations (41–43). We thus combined state-of-the-art AIMD using the revPBE0-D3 hybrid density functional for sampling of relevant structures with subsequent second-order Möller-Plesset perturbation theory (MP2) for VDE calculations. The latter calculations were performed for clusters carved out of the AIMD trajectory and embedded in a polarizable continuum model (PCM). See the supplementary materials for details.

AIMD simulations of an excess electron in bulk liquid ammonia demonstrate that an ammoniated electron occupies a cavity coordinated by ~12 ammonia molecules and has a gyration radius of 3.9 Å, on average (Fig. 2A), consistent with the value of ~3.5 Å from a moment analysis of the optical absorption spectra (52). The spin-paired ammoniated dielectron adopts a structure similar to that of the electron (Fig. 2B), with approximately the same number of ammonia molecules in contact and a slightly larger average gyration radius of 4.4 Å. In both cases, the solvent shell is very diffuse and lacks clear separation from the rest of the solvent. Our test AIMD calculations show that adding a second electron of the same spin leads to the formation of two separate solvated electron cavities rather than a dielectron in a single cavity.

The electron solvation structure in ammonia is qualitatively similar but quantitatively different from that of a hydrated electron in water or aqueous solution (33, 44). Namely, the first solvent shell of the hydrated electron is substantially more structured and less diffuse compared with those of the ammoniated electron or dielectron. Moreover, the hydrated electron is much smaller, with only

four to six water molecules in its hydration shell and a gyration radius of ~2.5 Å (44, 52). In regard to dielectrons, the situation in liquid ammonia is likely to be different from that in water, where hydrated dielectrons are predicted to be thermodynamically much less stable than hydrated electrons (53, 54).

The AIMD simulations also serve as a basis for calculations of the VDE of the ammoniated electron and dielectron. First, we carved out the immediate electron solvation shells containing 12 NH_3 molecules from more than 100 snapshots from the AIMD trajectories. These structures were then embedded in a PCM with the dielectric constant of liquid ammonia (see below and the supplementary materials for more details). The distributions of the resulting VDEs of the two species evaluated at the MP2 level (without any additional shifts or adjustments) are plotted in Fig. 3, referenced against our experimental data. The calculated distributions have widths of ~0.3 eV, peaking at ~2.0 eV for the ammoniated electron and ~1.6 eV for the dielectron. In comparison with our low-concentration experimental spectra, we see that the experimental peak at ~2 eV encompasses within its width both the calculated solvated electron and dielectron VDE distributions (Fig. 3). These results are consistent with the previously calculated very small difference of ~0.1 eV between the lowest optical transitions of an ammoniated electron and a spin-paired dielectron in an idealized six-coordinated cluster geometry (55). The value for the ammoniated electron, however, differs quantitatively from extrapolations from ammonia clusters with an excess electron (29), yielding 1.25 eV. This is due to the fact that the cryogenic clusters are finite and solid and, therefore, have different properties from those of the bulk liquid systems described here (56, 57).

Photoelectron spectroscopy: From electrolytes to metallic solutions

Upon increasing the alkali metal concentration, the PE spectra exhibit a gradual conversion of the Gaussian-type solvated electron peak into an asymmetric band with a sharp edge toward lower binding energies accompanied by one or two satellite peaks on the higher– binding energy side (Figs. 1 and 4, with details provided in the supplementary materials). At the lowest alkali metal concentrations, the solvated electron peak can be fitted to a Gaussian function (Fig. 4) with a full width at half maximum of about 0.45 to 0.6 eV [i.e., slightly narrower than the equivalent first ionization peak for halides in liquid ammonia (49)] and with a low energy onset (appearance potential) at ~1.5 eV, which is close to the previous estimate of 1.4 eV from the PE threshold measurements (24, 25).

By contrast, at the highest lithium concentration of 9.7 MPM, the PE spectrum is fitted to an inverse-parabola conduction band with a sharp Fermi edge and two plasmon peaks (Fig. 4), as follows directly from the free-electron gas model for metals (58), with an effective electron mass close to unity (Fig. 4 and Table 1). Owing to the relatively low electron density, the plasmon frequency is in the visible range, which gives the concentrated alkali metal–ammonia solutions their characteristic bronze or gold color (1, 59). A conduction band with a Fermi edge and a plasmon peak can also be observed for the 1.25 MPM potassium–ammonia solution, whereas for sodium–ammonia we could not prepare homogeneous solutions above ~1 MPM because of spontaneous phase separation at the experimental conditions (1, 2).

An analogous fit to a free-electron gas model is shown for a microjet PE spectrum of liquid 50/50 sodium–potassium metal alloy (Fig. 4A and Table 1). Here, the conduction band is wider and the fundamental plasmon excitation seen at higher binding energies has a higher frequency (~4.5 eV), as expected for the higher electron density in the metal alloy compared with the metallic lithium–ammonia solutions. The higher frequency places the plasmon in the ultraviolet range when considering the optical reflectance of the sodium– potassium alloy, which does not exhibit any color and has a metallic silver sheen. This is actually true for all alkali metals except cesium, in which the lower free-electron density shifts the plasmon frequency to the visible range, conferring a golden color (59).

The PE spectra of the ~1 to 4 MPM lithium– liquid ammonia solutions can be fitted by a combination of a localized Gaussian at 2 eV with a conduction band and plasmon following from a free-electron gas model, albeit with a reduced effective electron mass (Fig. 4D and Table 1). As the lithium concentration increases, the relative weight of the Gaussian contribution to the spectrum decreases such that, at 9.7 MPM, it practically vanishes (Fig. 4E). At the same time, the spectra exhibit changes in the shape and position of the liquid ammonia $3a_1$ peak upon buildup of the metallic behavior of the solution (Fig. 4C). Specifically, in the electrolyte regime the position of the $3a_1$ peak almost does not change, but it does tend to broaden and move to lower binding energies upon appearance of the metallic state (for more details, see the supplementary materials).

The above results suggest that, in accord with the previous view (1), the electrolyte-to- metal transition upon increasing the metal concentration in alkali metal–ammonia solutions is not a sharp phase transition but rather a gradual conversion that resembles a percolation process, with an unresolved question concerning the sizes of potentially coexisting microscopic regions supporting localized and delocalized electrons (2, 35, 60, 61). This is a different picture than that of a sharp transition at ~8 MPM drawn from recent PE spectra of alkali metal–ammonia nanodroplets (31). Although such experiments are pioneering in their own right, it is reasonable to question whether clusters of finite size are representative of bulk metallic solutions in their electronic structure. The cluster PE spectra exhibit notable differences, such as the lack of a sharp Fermi edge, the absence of plasmon peaks, and Fermi edge onset at higher rather than lower binding energies from the onset of the localized (di)electron peak (31). All of these factors suggest a qualitatively different transition in the nanodroplets, taking place at substantially higher concentrations, from those previously determined for bulk liquid systems (1, 31). Our present bulk liquid PES results show a buildup of a conduction band with a Fermi edge with increasing alkali metal concentration even before the solution becomes visibly metallic (Fig. 4). This picture is also in accord with the semiquantitative Mott's criterion, which postulates that a metallic state starts to appear when the mean distance between the electrons drops below approximately four times their size (62). With a ~4-Å radius of gyration of the ammoniated electrons and dielectrons (Fig. 2), metallic behavior should begin to evolve at ~1 MPM, which is consistent with the onset of conduction band

formation in the present PES measurements. Note, however, that the transition observed in this study is more gradual than what would strictly follow from a pure Mott's transition (62).

We can thus conclude that the occurrence in the PE spectrum of a conduction band with a distinct Fermi edge, together with plasmon peaks, is a signature of the electrolyte-to-metal transition. This gradual transition is observed in both the lithium–ammonia and potassium– ammonia solutions (see Figs. 1 and 4 and the supplementary materials). [As mentioned above, at concentrations exceeding ~1.5MPM, sodium–ammonia solutions phase-separate into immiscible electrolyte andmetallic phases (2), which compromises the microjet PE measurements.] One can also view the process from the other side—i.e., as a metal-to-electrolyte transition upon decreasing the alkali metal concentration. We see from Fig. 4 that, at the highest studied concentration of 9.7 MPM, themetallic lithium–ammonia systembehaves similarly to an ideal free-electron gas, as does the liquid sodium–potassium alloy or a pure alkalimetal (63, 64). However, upon decreasing the concentration of the alkali metal–ammonia solutions below ~4 MPM, we observe departure from the ideal electron gas model, as exemplified by a rapid decrease of the effective electron mass well below the value of 1 m_e (where m_e is the mass of a stationary electron); see Fig. 4D. A schematic is presented in Fig. 5 to capture the essence of the transition. This image depicts the gradual interconversion between localized "chemical" species (solvated electrons and dielectrons) and delocalized "physical" moieties (metallic conduction band electrons) upon changing the electron concentration.

Outlook

The present study shows that the electrolyteto- metal transition in increasingly concentrated alkali metal–liquid ammonia solutions is a gradual process rather than an abrupt first-order transition, which is in line with previous suggestions (1). From the molecular point of view, this transition may be understood in a simplifiedway as gradual coalescence of individual solvated electrons and dielectrons upon increasing alkali metal doping, with the metallic behavior appearing around the percolation threshold.

After overcoming methodological difficulties connected to modeling the onset of the metallic state, future AIMD simulations of concentrated alkali metal–liquid ammonia solutions will shed more light on the electrolyte-to-metal transition in terms of the underlying electronic structure and molecular geometries. On the experimental side, the experience already gained from studies of liquid ammonia microjets is proving essential in our current attempts to achieve the metallic state in the much more reactive (even explosive) alkali metal–water systems.

REFERENCES AND NOTES
1. E. Zurek, P. P. Edwards, R. Hoffmann, Angew. Chem. Int. Ed. 48, 8198–8232 (2009).
2. J. C. Thompson, Electrons in Liquid Ammonia (Clarendon Press, 1976).
3. M. T. Lodge et al., J. Phys. Chem. B 117, 13322–13334 (2013).
4. G. N. Chuev, P. Quémerais, J. Chem. Phys. 128, 144503 (2008).
5. G. N. Chuev, P. Quémerais, J. Crain, J. Chem. Phys. 127, 244501 (2007).
6. S. Hayama, N. T. Skipper, J. C. Wasse, H. Thompson, J. Chem. Phys. 116, 2991–2996 (2002).
7. H. Thompson et al., J. Am. Chem. Soc. 125, 2572–2581 (2003).
8. J. Kohanoff, F. Buda, M. Parrinello, M. L. Klein, Phys. Rev. Lett. 73, 3133–3136 (1994).
9. T. A. Kaplan, J. F. Harrison, J. L. Dye, R. Rencsok, Phys. Rev. Lett. 75, 978 (1995).
10. C. A. Burns, E. D. Isaacs, P. Abbamonte, P. M. Platzman, J. Phys. Chem. Solids 61, 411–413 (2000).
11. G. Lepoutre, M. J. Sienko, Eds., Solutions Metal-Ammoniac: Proprietes Physico-Chimiques (Benjamin, 1964).
12. J. J. Lagowski, M. J. Sienko, Eds., Metal–Ammonia Solutions (Butterworths, 1970).
13. J. Jortner, N. R. Kestner, Eds., Electrons in Fluids (Springer, 1973).
14. B. Webster, J. Phys. Chem. 84, 1065–1069 (1980).
15. G. Lepoutre, J. Phys. Chem. 88, 3699–3700 (1984).
16. F. Leclercq, P. Damay, J. Phys. IV 1, R7 (1991).
17. P. P. Edwards, J. Phys. Chem. 88, 3772–3780 (1984).
18. M. C. R. Symons, Chem. Soc. Rev. 5, 337–358 (1976).
19. I. A. Shkrob, J. Phys. Chem. A 110, 3967–3976 (2006).
20. P. E. Mason et al., Nat. Chem. 7, 250–254 (2015).
21. D. M. Neumark, Nat. Chem. 2, 247–248 (2010).
22. Y. Tang et al., Phys. Chem. Chem. Phys. 12, 3653–3655 (2010).
23. F. Buchner, T. Schultz, A. Lübcke, Phys. Chem. Chem. Phys. 14, 5837–5842 (2012).
24. J. Häsing, Ann. Phys. 429, 509–533 (1940).
25. H. Aulich, B. Baron, P. Delahay, R. Lugo, J. Chem. Phys. 58, 4439–4443 (1973).
26. T. Teherani, K. Itaya, A. J. Bard, N. J. Chimie 2, 481–487 (1978).
27. H. Haberland, C. Ludewigt, H. G. Schindler, D. R. Worsnop, Surf. Sci. 156, 157–164 (1985).
28. R. Takasu, F. Misaizu, K. Hashimoto, K. Fuke, J. Phys. Chem. A 101, 3078–3087 (1997).
29. H. W. Sarkas, S. T. Arnold, J. G. Eaton, G. H. Lee, K. H. Bowen, J. Chem. Phys. 116, 5731–5737 (2002).
30. T. Zeuch, U. Buck, Chem. Phys. Lett. 579, 1–10 (2013).
31. S. Hartweg, A. H. C. West, B. L. Yoder, R. Signorell, Angew. Chem. Int. Ed. 55, 12347–12350 (2016).
32. O. Marsalek, F. Uhlig, P. Jungwirth, J. Phys. Chem. C 114, 20489–20495 (2010).
33. O. Marsalek, F. Uhlig, J. VandeVondele, P. Jungwirth, Acc. Chem. Res. 45, 23–32 (2012).
34. T. E. Gartmann et al., Phys. Chem. Chem. Phys. 20, 16364–16371 (2018).
35. P. Vöhringer, Ann. Rev. Phys. Chem. 66, 97–118 (2015).
36. T. Vogler, P. Vöhringer, Phys. Chem. Chem. Phys. 20, 25657–25665 (2018).
37. J. Lindner, A.-N. Unterreiner, P. Vöhringer, ChemPhysChem 7, 363–369 (2006).
38. J. Lindner, A.-N. Unterreiner, P. Vöhringer, J. Chem. Phys. 129, 064514 (2008).
39. T. Buttersack et al., J. Am. Chem. Soc. 141, 1838–1841

(2019).

40. B. Winter et al., J. Phys. Chem. A 108, 2625–2632 (2004).

41. Z. Deng, G. J. Martyna, M. L. Klein, Phys. Rev. Lett. 71, 267–270 (1993).

42. Z. H. Deng, G. J. Martyna, M. L. Klein, J. Chem. Phys. 100, 7590–7601 (1994).

43. G. J. Martyna, Z. H. Deng, M. L. Klein, J. Chem. Phys. 98, 555–563 (1993).

44. F. Uhlig, O. Marsalek, P. Jungwirth, J. Phys. Chem. Lett. 3, 3071–3075 (2012).

45. R. Seidel, M. N. Pohl, H. Ali, B. Winter, E. F. Aziz, Rev. Sci. Instrum. 88, 073107 (2017).

46. K. J. S. Sawhney, F. Senf, W. Gudat, Nucl. Instrum. Methods Phys. Res. A 467–468, 466–469 (2001).

47. B. Winter, M. Faubel, Chem. Rev. 106, 1176–1211 (2006).

48. M. N. Pohl et al., Chem. Sci. 10, 848–865 (2018).

49. T. Buttersack et al., Rev. Sci. Instrum. 91, 043101 (2020).

50. U. Schindewolf, M. Werner, J. Phys. Chem. 84, 1123–1127 (1980).

51. T. Sommerfeld, K. M. Dreux, J. Chem. Phys. 137, 244302 (2012).

52. S. Golden, T. R. Tuttle, J. Chem. Soc., Faraday Trans. II 75, 474–484 (1979).

53. R. E. Larsen, B. J. Schwartz, J. Phys. Chem. B 110, 1006–1014 (2006).

54. K. H. Schmidt, D. M. Bartels, Chem. Phys. 190, 145–152 (1995).

55. M. Mauksch, S. B. Tsogoeva, Phys. Chem. Chem. Phys. 20, 27740–27744 (2018).

56. O. Marsalek, F. Uhlig, T. Frigato, B. Schmidt, P. Jungwirth, Phys. Rev. Lett. 105, 043002 (2010).

57. L. Ma, K. Majer, F. Chirot, B. von Issendorff, J. Chem. Phys. 131, 144303 (2009).

58. C. Kittel, Introduction to Solid State Physics (Wiley, 2005).

59. C. C. Addison, The Chemistry of Liquid Alkali Metals (Wiley, 1984).

60. J. Jortner, M. H. Cohen, Phys. Rev. B 13, 1548–1568 (1976).

61. P. Damay, P. Chieux, J. Phys. Chem. 84, 1203–1205 (1980).

62. P. P. Edwards, M. T. J. Lodge, F. Hensel, R. Redmer, Philos. Trans. R. Soc. A 368, 941–965 (2010).

63. G. Indlekofer, P. Oelhafen, J. Non-Cryst. Solids 117–118, 340–343 (1990).

64. G. Indlekofer, P. Oelhafen, J. Non-Cryst. Solids 156–158, 226–231 (1993).
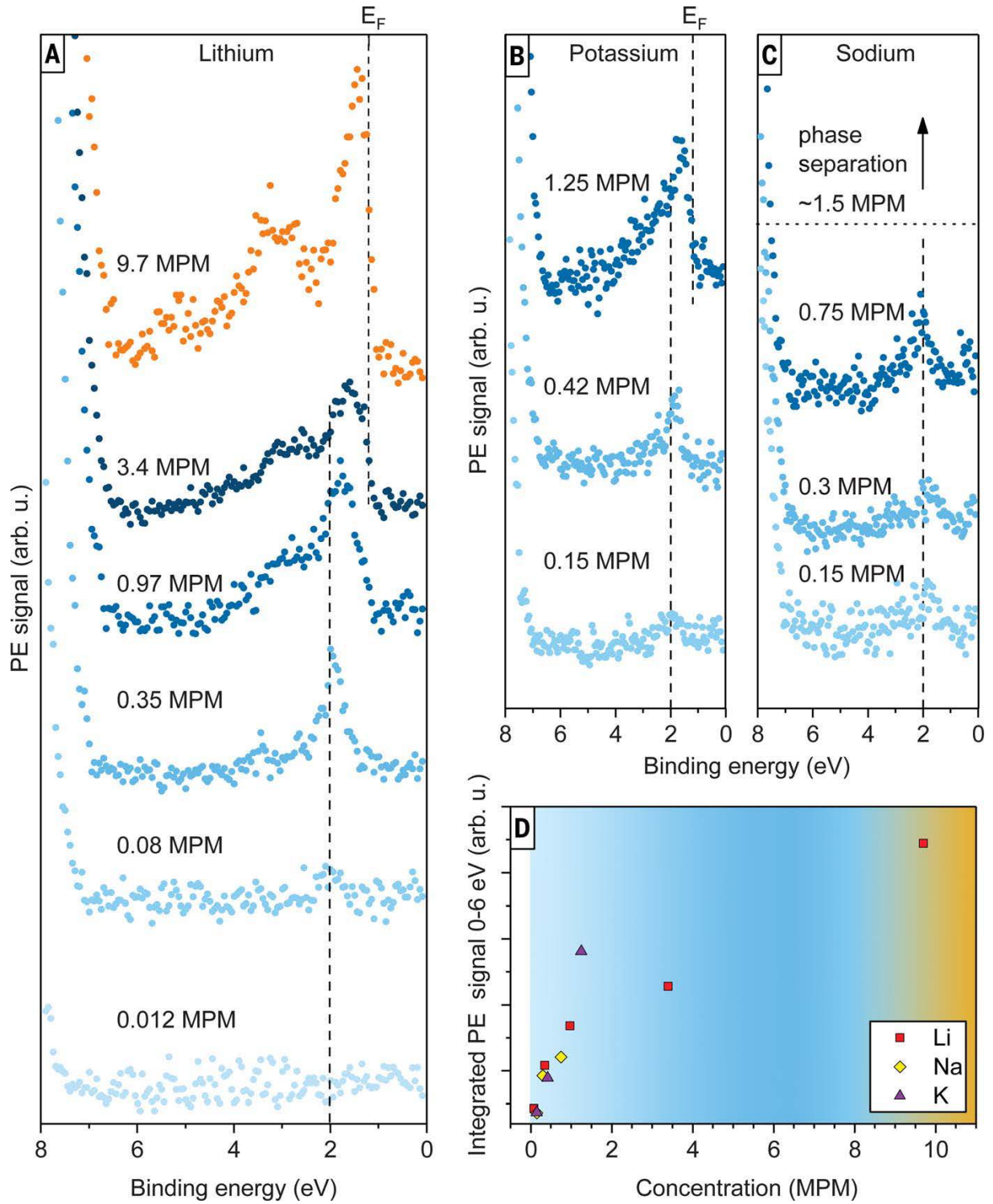
Fig. 1. Experimental PE spectra of alkali metal–liquid ammonia solutions at various concentrations, as obtained by synchrotron x-ray PES in a refrigerated liquid microjet setup. (A) Li in NH_3, (B) K in NH_3, and (C) Na in NH_3. Individual data points are color-coded to reflect the actual color of the solutions. Energy scales are shown with respect to the vacuum level. (D) Integrated peak areas from 0 to 6 eV in (A) (red), (B) (purple), and (C) (yellow), as a function of alkali metal concentration. arb. u., arbitrary units.
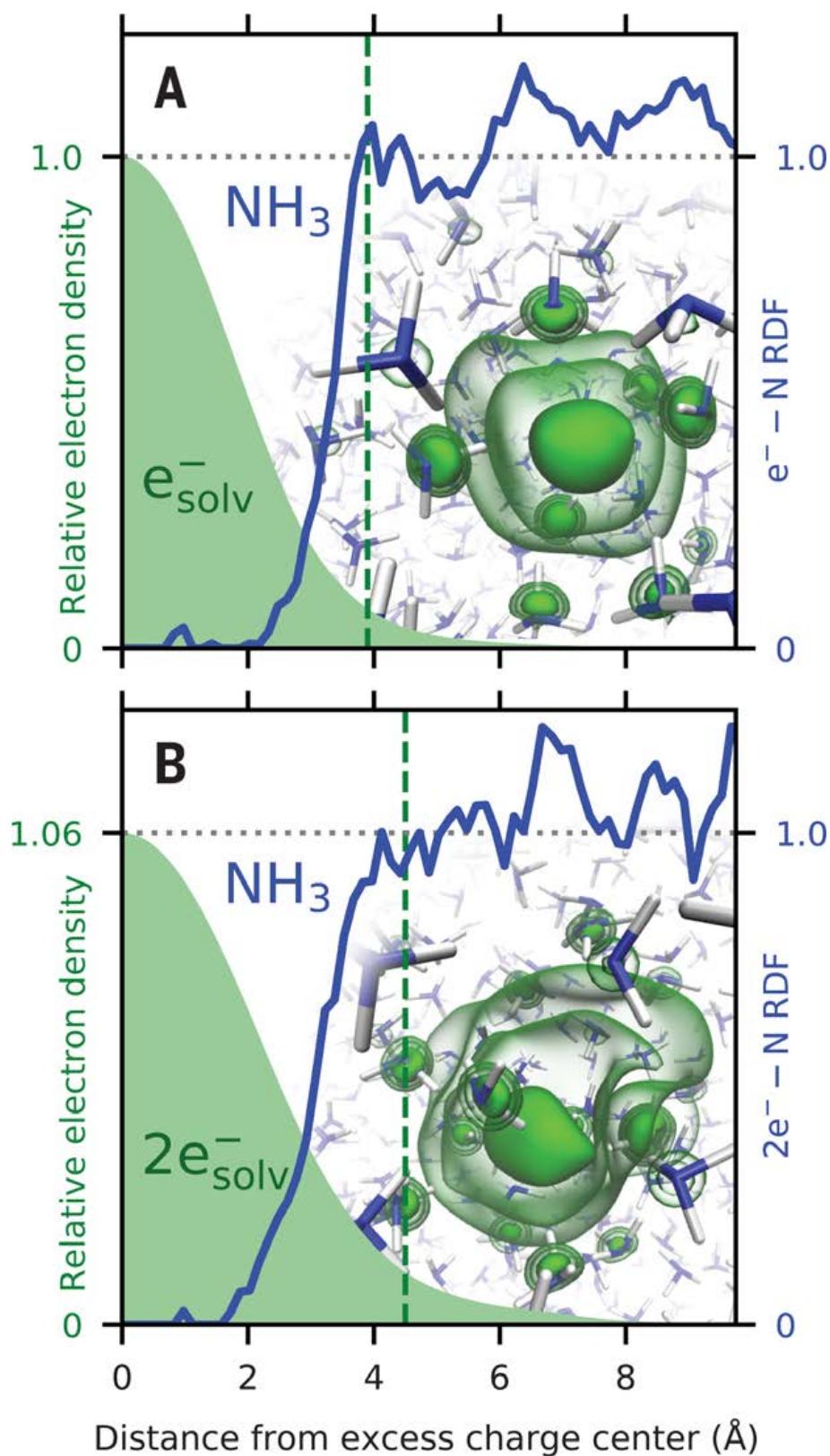
Fig. 2. Ammoniated electron and dielectron simulated by ab initio molecular dynamics (AIMD). AIMD results for (A) the ammoniated electron and (B) the ammoniated dielectron. Radial electron density profiles were calculated from the squares of the corresponding Wannier orbitals (green filled curves) and the center of excess charge—ammonia nitrogen radial distribution functions (RDF) (blue curves). Normalization is such that the integrated excess electron density of the dielectron is twice that of the electron (the latter being arbitrarily set to peak at the value of 1). Dashed vertical lines denote the electron or dielectron radius of gyration. Inset images depict the squared Wannier orbitals with surrounding ammonia molecules in the AIMD simulation box. e^-_{solv}, solvated electron.
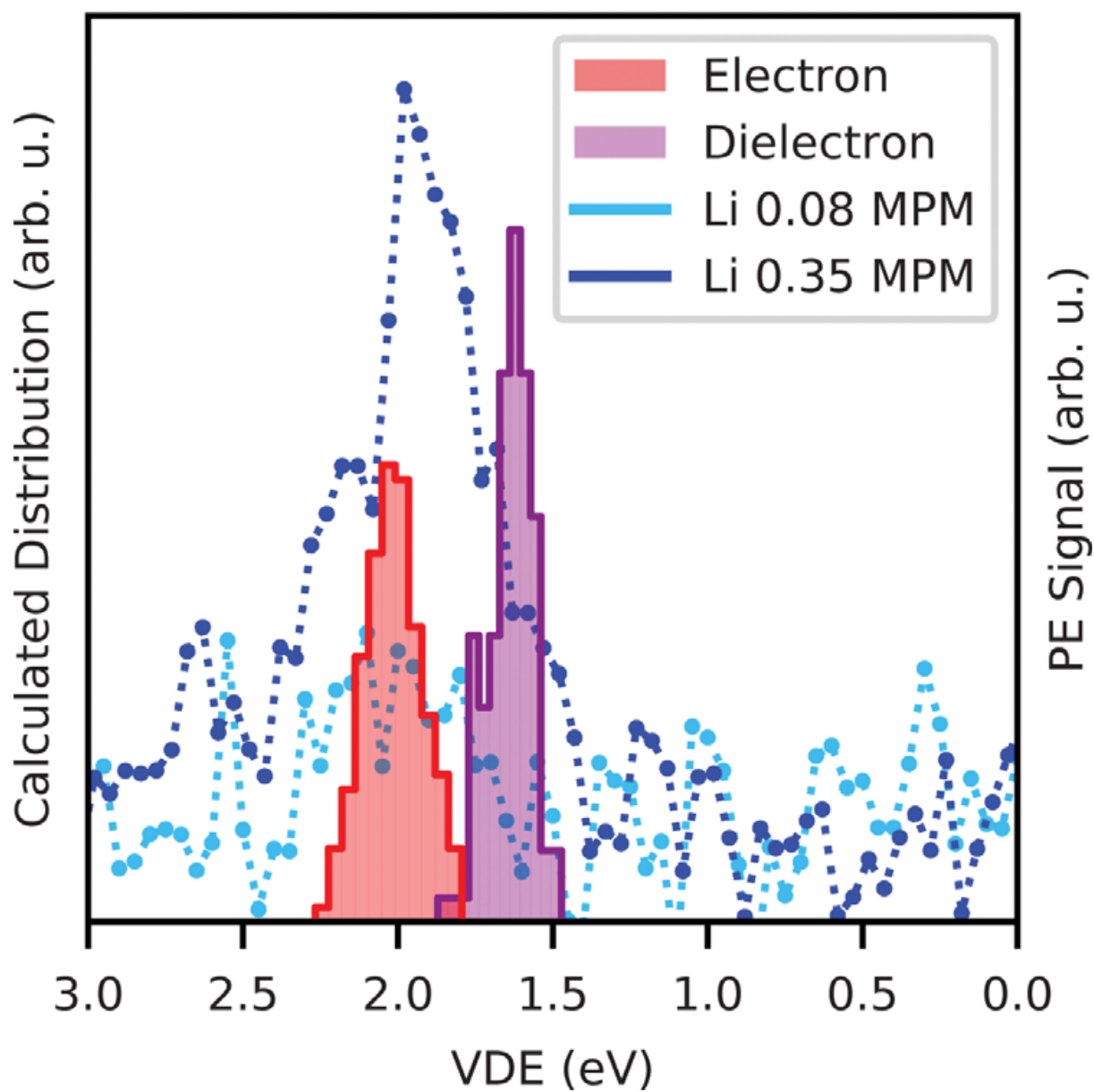
Fig. 3. Simulated VDE. An ammoniated electron (red) and dielectron (purple) were modeled using solvation shells with 12 ammonia molecules carved out from AIMD simulations and embedded in a PCM. For comparison, the corresponding experimental PE spectra of the low-concentration lithium–ammonia solutions (from Fig. 1A) are shown.
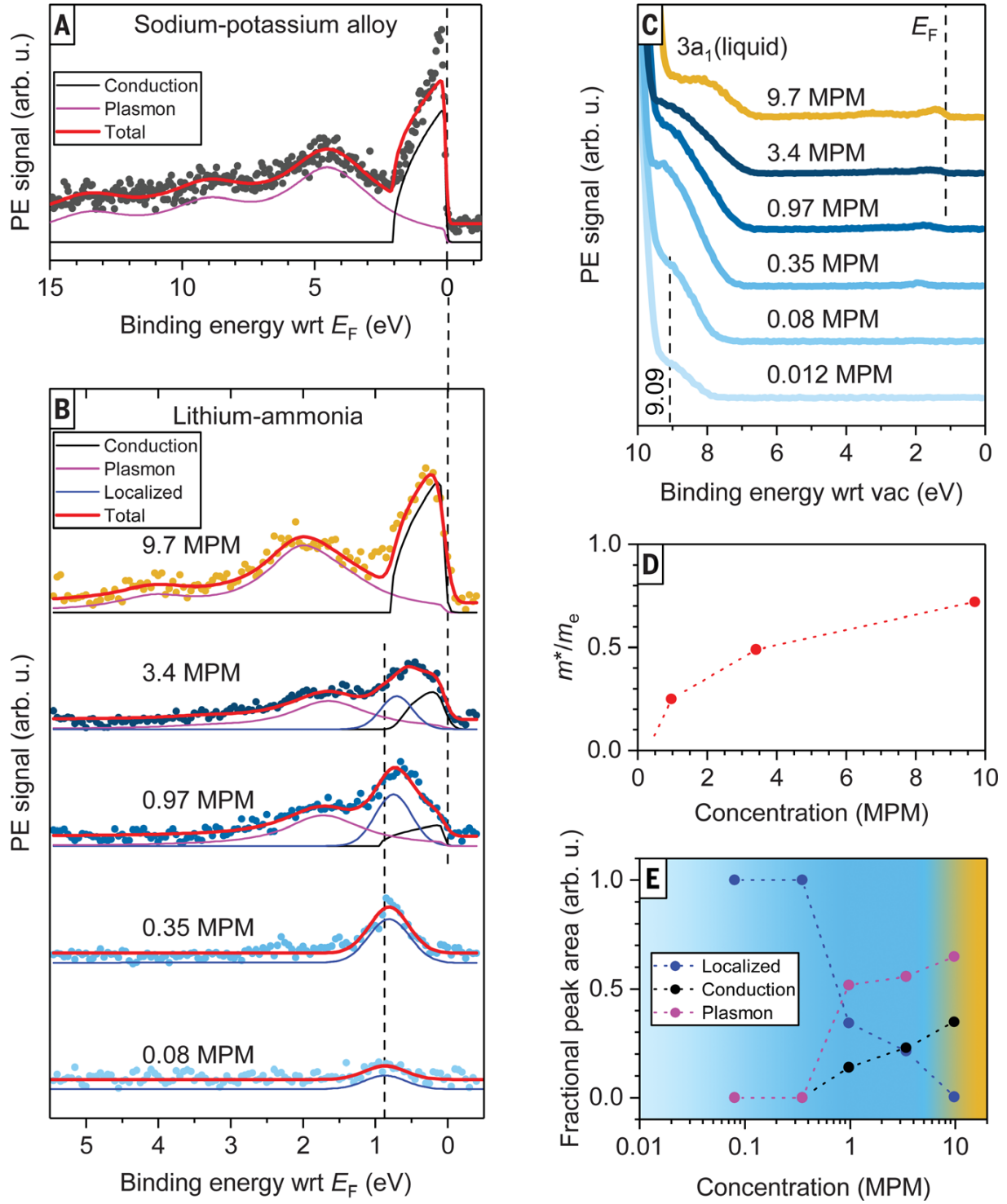
Fig. 4. Analysis and fits of the PE spectra in the electrolyte and metallic regimes. Partial fits to the conduction band, plasmons, and localized (di)electrons are vertically offset for visual clarity. (A) Fit (relative root mean square error of 5.3%) of the liquid Na–K alloy to a free-electron gas model. At low binding energy, we observe a Fermi edge leading feature with the characteristic parabolic shape of the conduction band; plasmon excitations are seen at higher binding energies. (B) Fits (relative root mean square errors of 6.3, 6.8, 7.1, 8.9, and 32.2% for 9.7, 3.4, 0.97, 0.35, and 0.08 MPM, respectively) of Li–NH$_3$ data to a combination, in varying ratios, of a free-electron gas model with plasmon bands for the fraction where the electron is delocalized and a single Gaussian function to represent the localized (di)electron. (C) Evolution of the liquid ammonia 3a$_1$ peak upon increasing Li concentration. (D) Concentration dependence of the effective electron mass from fits in (A) and (B). (E) Relative peak areas corresponding to the localized Gaussian, the conduction band, and the plasmon peaks in (B). wrt, with respect to; E$_F$, Fermi energy; vac, vacuum; m*, effective electron mass; m$_e$, stationary electron mass.

Table 1. Key parameters for lithium–ammonia solutions and the sodium–potassium alloy. c, concentration; n_e, electron density; m_e^*, effective electron mass; m_e, stationary electron mass. Widths of the conduction band (E_c) and positions of the plasmon peak (E_P) are expressed with respect to the Fermi energy (E_F). E_c and E_P were determined from fitting to a free-electron gas model with the effective electron masses given in the table. The effective electron masses m_e^* were obtained by fitting as described in the supplementary materials. –, not determined.

	NaK	Li@NH$_3$	Li@NH$_3$	Li@NH$_3$	Li@NH$_3$	Li@NH$_3$	Li@NH$_3$
c (MPM)	100	9.7	3.4	0.97	0.35	0.08	0.012
c (M)	29	4.3	1.4	0.39	0.14	0.03	0.005
n (10^{21} cm^{-3})	16.3	2.15	1.05	0.25	0.09	0.02	0.003
m_e^*/m_e	1.21	0.72	0.49	0.25	---	---	---
E_c (eV)	2.06	0.85	0.74	0.98	---	---	---
E_p (eV)	4.52	2.03	1.67	1.74	---	---	---